

# Giant Tunneling Electroresistance Induced by Interfacial Doping in Pt/BaTiO<sub>3</sub>/Pt Ferroelectric Tunnel Junctions

Wei Xiao<sup>1,2,3</sup> Lili Kang,<sup>4</sup> Hua Hao,<sup>1</sup> Yanhong Zhou,<sup>5</sup> Xiaohong Zheng,<sup>1,2,3,\*</sup> Lei Zhang<sup>6,7,†</sup> and Zhi Zeng<sup>1,2</sup>

<sup>1</sup>Key Laboratory of Materials Physics, Institute of Solid State Physics, HFIPS, Chinese Academy of Sciences, Hefei 230031, China

<sup>2</sup>Science Island Branch of Graduate School, University of Science and Technology of China, Hefei 230026, China

<sup>3</sup>College of Information Science and Technology, Nanjing Forestry University, Nanjing 210037, China

<sup>4</sup>Institute for Computational Materials Science, School of Physics and Electronics, Henan University, Kaifeng 475004, China

<sup>5</sup>College of Science, East China Jiao Tong University, Nanchang, Jiangxi 330013, China

<sup>6</sup>State Key Laboratory of Quantum Optics and Quantum Optics Devices, Institute of Laser Spectroscopy, Shanxi University, Taiyuan 030006, China

<sup>7</sup>Collaborative Innovation Center of Extreme Optics, Shanxi University, Taiyuan 030006, China

(Received 20 October 2021; revised 7 February 2022; accepted 11 March 2022; published 1 April 2022)

Ferroelectric tunnel junctions (FTJs) are very promising candidates for nonvolatile memory devices and a large tunneling electroresistance (TER) ratio is essential for their high performance. This work intends to achieve large TER ratio by interfacial doping in FTJs by taking Pt/BaTiO<sub>3</sub>/Pt tunnel junctions as an example. By introducing Na (or Li) substitutions for Ti atoms at the right interface, the resultant strong Coulomb repulsion from the negatively charged NaO<sub>2</sub> interface pushes the electrons to higher energy in an increasing manner from left to right in the whole BaTiO<sub>3</sub> barrier, which leads to rapidly increasing potential energy profile and partial metallization close to the right interface in the left polarization state. However, in the right polarization state, since the right ferroelectric polarization produces a decreasing potential energy profile from left to right, although the NaO<sub>2</sub> interface also pushes the electrons to much higher energy and the slope of the potential energy profile changes from negative to positive, the final slope of the potential energy profile is much less steeper and the Fermi level is always inside the band gap, leading to a completely insulating state. The substantially different distributions of the electrostatic potential energy profile in the two polarization states lead to great differences in the transport properties. Based on density-functional-theory calculations, a TER ratio up to 10<sup>5</sup>% is achieved. The results indicate that a negatively charged interface based on interfacial substitution is a promising method for obtaining a large TER ratio in FTJs, and thus will have implications for the further understanding and design of high-performance FTJs.

DOI: 10.1103/PhysRevApplied.17.044001

## I. INTRODUCTION

Ferroelectric tunnel junctions (FTJs), which are made of ferroelectric thin films sandwiched between two metal electrodes have great technological applications in non-volatile random access memories [1–9]. However, the study of FTJs had made little progress in the 30 years after it was initially proposed by Esaki in the 1970s as a concept of polar switch [10]. Nevertheless, since the existence of nanoscale ferroelectricity in thin films has been proved in 2003 [11–13], the FTJs have been widely studied.

The FTJs have many advantages over other forms of memory devices constructed with ferroelectric materials. For example, unlike the destructive readout of commercial ferroelectric random access memories [14], the FTJs achieve a nondestructive readout by reading the conductance of the tunnel junction to obtain the written resistance states. Moreover, although ferroelectric diodes have the characteristic of nondestructive readout [15,16], the thick ferroelectric layer limits their miniaturization. In contrast, the thickness of the ferroelectric layer of the FTJs is reduced to a few nanometers, which is conducive to its miniaturization. In addition, the FTJs are also characterized by the high density of data storage, high speed of read and erase, and low power consumption, which have attracted

\*xhzheng@theory.issp.ac.cn

†zhanglei@sxu.edu.cn

extensive research interest in recent years. For the study of FTJs, a very useful parameter of performance is the tunnel electroresistance (TER) ratio, which measures the change in the resistance of the tunnel junctions with ferroelectric polarization reversal under the external electric field. The TER effect in FTJs has been widely demonstrated by theories [2,3,17–19] and experiments [4,5,20–26], and great efforts have been made to achieve a giant TER ratio.

Various approaches involving the modulation of the ferroelectric barrier have been proposed to achieve the TER effect. Zhuravlev *et al.* studied the variation of ferroelectric barrier height in tunnel junctions with metal electrodes of different screening lengths under polarization reversal by using the Thomas-Fermi model of screening [27] in 2005 and, thus, obtained the TER effect [2]. Also, using electrodes with different screening lengths, Chanthbouala *et al.* experimentally modulated the height of the barrier and obtained a TER ratio of approximately 10<sup>4</sup>% [4]. In addition, by choosing appropriate ferroelectric materials to increase the intensity of ferroelectric polarization [28,29] or by adjusting the work function of the metal electrodes [30], the height of the ferroelectric barrier can also be changed to achieve large TER effect. According to the basic quantum mechanics, the tunneling transmittance depends exponentially on the height and width of the barrier with the relation  $T \sim \exp(-d\sqrt{\phi})$ , where  $T$  is the transmittance,  $d$  the barrier width, and  $\phi$  the barrier height [31]. Therefore, the ferroelectric barrier width is also a degree of freedom to tune the TER feature of the tunnel junction. For example, by increasing the thickness of ferroelectric material BaTiO<sub>3</sub>(1–3 nm) in tunnel junction, Garcia *et al.* increased the TER ratio from 30% to 750% [20]. Other methods, such as considering the band alignment between electrodes and ferroelectric material [32] or applying the converse piezoelectric effect [3,33,34], can also be used to adjust the width of the ferroelectric barrier to obtain the TER effect.

In addition, there are still other ways to obtain the TER effect that go beyond controlling the height and width of the ferroelectric barrier. For example, because the strong correlation electron oxide La<sub>1-x</sub>A<sub>x</sub>MnO<sub>3</sub> (A = Sr, Ca, or Ba) can undergo a series of phase transitions when the carrier concentration changes [35,36], and the carrier concentration can be tuned by ferroelectric polarization [37], these kinds of materials have attracted extensive attention. Yin *et al.* studied the LSMO/BaTiO<sub>3</sub>/La<sub>0.5</sub>Ca<sub>0.5</sub>MnO<sub>3</sub>/LSMO (LSMO = La<sub>0.7</sub>Sr<sub>0.3</sub>MnO<sub>3</sub>) tunnel junction and realized the TER ratio of approximately 10<sup>4</sup>% by utilizing the transition between ferromagnetic metal and antiferromagnetic insulating phase of the interlayer (La<sub>0.5</sub>Ca<sub>0.5</sub>MnO<sub>3</sub>) under ferroelectric polarization reversal [38]. Using the correlated electron oxide (CEO) La<sub>1-x</sub>Sr<sub>x</sub>MnO<sub>3</sub> as the electrode, Jiang *et al.* realized the TER ratio of approximately 3.0 × 10<sup>4</sup>% with the optimal thickness (7 nm) of ferroelectric

material PbZr<sub>0.2</sub>Ti<sub>0.8</sub>O<sub>3</sub> under the phase transition of the CEO [39]. Similarly, Radaelli *et al.* also realized the enhanced TER effect in Pt/La<sub>0.5</sub>Sr<sub>0.5</sub>MnO<sub>3</sub>/BaTiO<sub>3</sub>/LSMO tunnel junction [40]. In addition to the metal-insulation phase transition, the use of an *n*-type semiconductor as the electrode to obtain the Schottky barrier [23,26,41], the use of ion migration [5,42–44], and the use of composite barriers [24,45–48] have all been reported to achieve the TER effect.

In addition, substitutional doping [49–53] has proven to be an effective way to control electronic transport. For example, Wang *et al.* studied this effect in Pt/SrTiO<sub>3</sub>/Pt heterostructure and found that by substituting the La<sup>3+</sup> for Sr<sup>2+</sup> and the Nb<sup>5+</sup> for Ti<sup>4+</sup> in SrTiO<sub>3</sub>, the originally closed conductance channel can be opened. However, with the substitution of Ba<sup>2+</sup>(or Ca<sup>2+</sup>) for Sr<sup>2+</sup> and Hf<sup>4+</sup> for Ti<sup>4+</sup>, the conductance channel remains closed [54]. More interestingly, Klyukin *et al.* also worked on the Pt/SrTiO<sub>3</sub>/Pt tunnel junction by substituting Ti for Sr inside the paraelectric SrTiO<sub>3</sub> barrier and obtained local polarization around the dopants and a LDOS peak inside the band gap, which mediates the electron transport. The direction of the local polarization can be reversed under external electrical field, which leads to the different positions of the LDOS peak from the Fermi level and finally a TER ratio of approximately 10<sup>4</sup>% [55]. Inspired by the doping effects in these studies, we believe that interfacial doping at only one interface of a symmetric FTJ may break the symmetry of electrostatic potential distribution and different electrostatic potential distribution under ferroelectric polarization reversal may be achieved, which may lead to a large TER ratio. As a matter of fact, in this work, by taking Pt/BaTiO<sub>3</sub>/Pt FTJ as an example and substituting Ti with Na (or Li) at the right (namely, BaTiO<sub>3</sub>/Pt) interface, accompanied by the substantially different electrostatic distribution under ferroelectric polarization reversal and the appearance and disappearance of partial metallization in the two polarization states resulting from the Coulomb repulsion of the negatively charged NaO<sub>2</sub> layer, a TER ratio of up to approximately 10<sup>5</sup>% is achieved, based on density-functional-theory (DFT) calculations.

## II. COMPUTATION DETAILS

The central region of the FTJ is chosen by stacking 4.0 unit cells (u.c.) of Pt, 8.5 u.c. (or 9.5 u.c.) of BaTiO<sub>3</sub>, and 4.5 u.c. of Pt along the [001] direction, with the substitution of Na or Li for Ti (Na<sub>Ti</sub> or Li<sub>Ti</sub>) at the right interface [see Figs. 1(a), 6(a), and Fig. S6(a) within the Supplemental Material [56]]. The interface between the ferroelectric barrier and the electrodes on both sides is taken to be the same, namely, the most stable TiO<sub>2</sub>/Pt interface [57], which is specially used to study the effect of substitution atoms on the whole electrostatic potential distribution of the FTJ. The in-plane lattice constant

of the supercell is constrained to 3.991 Å, which is the experimental value of bulk BaTiO<sub>3</sub> [58]. The atomic coordinates within the supercell and the out-of-plane lattice constant are completely relaxed. By setting the  $z$  displacements between Ti and its adjacent O as positive or negative values before structural relaxation, two polarization states of FTJ structure are obtained after optimizing the structure. The  $c/a$  value of the tetragonal BaTiO<sub>3</sub> generated in FTJ after the optimization of the structure is greater than 1.0, which will produce a polar displacement perpendicular to the interface. Structural optimization is performed by the DFT-based SIESTA package [59,60], and Perdew-Burke-Ernzerhof (PBE) generalized gradient approximation (GGA) is used for the exchange correlation functional [61]. The mesh cutoff energy is set to 250 Ry to define the plane-wave cutoff for the grid, and the basis sizes adopt the double  $\zeta$  basis plus polarization orbitals (DZP) for all the elements. A relatively sparse  $5 \times 5 \times 1$  Monkhorst-Pack  $k$ -sampling grid is used for atomic relaxation calculations as the accuracy for this step in the  $x$ - $y$  plane is less relevant. The coordinates are optimized until the maximum atomic force is smaller than 0.04 eV/Ang. The self-consistent calculations are performed with a finer  $k$ -sampling grid of  $9 \times 9 \times 1$ . The TranSIESTA method [62,63] is used to calculate the self-consistent electron density and electrostatic potential of the two-probe open system and tight-binding transport (TBtrans) code [62,63] based on the nonequilibrium Green's function formalism is used to calculate the transport properties of the system. A  $k$ -point mesh of  $100 \times 100$  is chosen to sample the two-dimensional Brillouin zone for calculating the transmission functions. From the transmission function  $T(E)$ , we can get the equilibrium conductance  $G = T(E_F)G_0$ , with  $E_F$  the Fermi energy of the leads and  $G_0 = 2e^2/h$  the quantum conductance. To test the accuracy of the parameters, as an example, we try the energy cutoff of 400 Ry and  $6 \times 6 \times 1$   $k$ -sampling grid for the structure relaxation of the left polarization state. Compared with the parameters of 250 Ry and  $5 \times 5 \times 1$   $k$ -sampling grid, we find that the maximum change of the atomic coordinates is only 0.06 Å, about 1.5% of the in-plane lattice constant 3.991 Å, which leads to negligible change in the transmission around the Fermi level. Thus, our results are presented all with 250 Ry and  $5 \times 5 \times 1$   $k$ -sampling grid to save computation time.

### III. RESULTS AND DISCUSSION

The fully optimized atomic structures in the two polarization states for Na<sub>Ti</sub>-FTJ with 8.5 u.c. BaTiO<sub>3</sub> are shown in Fig. 1(a). From the lower arrows showing the local polarization of the two polarization states, it is seen that there is an anomalous polarization reversal for the nearest region of the substituted Na atom in the left polarization state. This phenomenon is also observed in the Ti-O displacement diagram drawn in Fig. 1(b), where positive

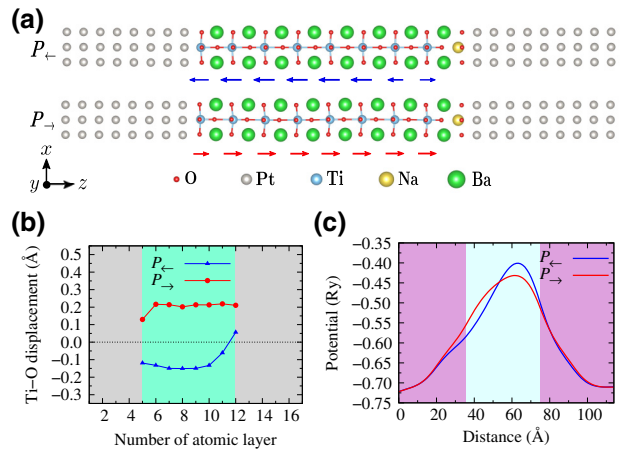


FIG. 1. Structural and electrical polarization properties for the Na<sub>Ti</sub>-FTJ with 8.5 u.c. BaTiO<sub>3</sub>. (a) Schematic diagram of optimized atomic structure for the left polarization state ( $P_{\leftarrow}$ , top panel) and the right polarization state ( $P_{\rightarrow}$ , bottom panel). The blue and red arrows indicate the local polarization of BaTiO<sub>3</sub> in the two polarization states. (b) The relative polar displacement between cation Ti<sup>4+</sup> and anion O<sup>2-</sup> in each atomic layer. (c) The averaged electrostatic potential distribution (in energy unit) of the whole tunnel junction along the  $z$  direction.

and negative Ti-O displacements simultaneously appear on the right side of the left polarization state. This is due to the substitution of Na for Ti, which causes the original electrically neutral TiO<sub>2</sub> interface to become a negatively charged one. Such an interface will generate an attractive effect on the surrounding cations Ti<sup>4+</sup>, and the nearest cation Ti<sup>4+</sup> will feel the strongest attraction. This will keep the polarization of the region closest to the substituted Na atom from being reversed, thus, the local polarization will be opposite to the bulk polarization in the left polarization state. Consequently, the region closest to the substituted Na atom forms a tail-to-tail ferroelectric domain wall, as observed in other systems [64]. The Coulomb repulsion between the negative ferroelectric bound charges at the domain wall and the negatively charged NaO<sub>2</sub> interface will result in a higher electrostatic potential profile on the right side of the ferroelectric barrier for the left polarization state [Fig. 1(c), blue line]. Unlike the left polarization state, the right polarization state is almost uniformly polarized and no domain wall is formed. It is shown in Fig. 1(b) that the Ti-O displacement is positive throughout the tunnel junction. Since the positive ferroelectric bound charges at the right interface cancel out with the negative NaO<sub>2</sub> interface, the electrostatic potential profile of ferroelectric barrier for the right polarization state [Fig. 1(c), red line] is much less steep than that of the left polarization state. We predict that the different distribution of electrostatic potential in the two polarization states will produce an interesting difference in the transport properties, which is studied below.

To evaluate the stability of the two polarization states with right interface doping and the energy barriers switching between them, we carry out a series of static calculations for the two polarization states of the  $\text{Na}_{\text{Ti}}\text{-FTJ}$  with 8.5 u.c.  $\text{BaTiO}_3$  by using the linear interpolation method of atomic coordinates [ $z(\lambda) = (1 - \lambda)z(P_{\leftarrow}) + \lambda z(P_{\rightarrow})$ ]. By varying the value of  $\lambda$ , the left polarization state is represented when  $\lambda = 0$ , and the right polarization state is represented when  $\lambda = 1$ . Figure 2(a) shows the feasibility of switching between the two polarization states for this tunnel junction under an applied electric field due to the fact that both polarization states fall at the local minimum. After analyzing the data, we get that the depth of the potential well for the left polarization state is about 0.179 eV (between  $\lambda = 0.0$  and 0.3), and for the right polarization state is about 1.811 eV (between  $\lambda = 1.0$  and 0.3). This bistable electrical modulation is one of the useful characteristics of the FTJs as nonvolatile memory devices. For the shallower potential well in the left polarization state, better stability can be obtained by increasing the thickness of the ferroelectric barrier as discussed later for the  $\text{Na}_{\text{Ti}}\text{-FTJ}$  with 9.5 u.c.  $\text{BaTiO}_3$ .

For the above bistable configuration, we calculate the transmission properties of the two polarization states for  $\text{Na}_{\text{Ti}}\text{-FTJ}$  with 8.5 u.c.  $\text{BaTiO}_3$ . From the calculated transmission functions in the energy range of  $-0.6$  to  $0.6$  eV in Fig. 2(b), we obtain the tunneling equilibrium conductance values for the left and right polarization states as  $G_{\leftarrow} \sim 1.248 \times 10^{-8} G_0$  and  $G_{\rightarrow} \sim 9.726 \times 10^{-12} G_0$ , where  $G_0 = 2e^2/h$  is the conductance quantum, with  $e$  the electron charge and  $h$  Plank's constant. The TER ratio, which is quantified as  $\text{TER} = |G_{\leftarrow} - G_{\rightarrow}|/\min(G_{\leftarrow}, G_{\rightarrow})$  under polarization reversal, reaches approximately  $1.282 \times 10^{5}\%$ . The decrease in tunneling

conductance from the left polarization state to the right polarization state can also be seen from the calculated  $k_{\parallel}$ -resolved transmission in the two-dimensional Brillouin zone (2DBZ) at the Fermi energy as shown in Fig. 2(c). For the left polarization state, the transmission region is concentrated in the bright red large circular region of the 2DBZ. The transmission is considerably enhanced near the  $\bar{\Gamma}$  point ( $k_{\parallel} = 0$ ) in the 2DBZ. For the right polarization state, the reduced transmission is obviously observed in the bright yellow large circular region of the 2DBZ. The shape of the large transmission area in the left and right polarization state in Fig. 2(c) is derived from the high density area of Bloch states of the bulk metal Pt electrode as shown in Fig. 2(d).

To gain a deep understanding of the large tunneling conductance difference between the left and right polarization states, we calculate the layer-resolved density of states (DOS) for the  $\text{Na}_{\text{Ti}}\text{-FTJ}$  with 8.5 u.c.  $\text{BaTiO}_3$ . As seen from Fig. 3(a), compared with the relatively flat distribution of the DOS in the right polarization state, the distribution of DOS for the left polarization state shifts upward from left to right, with a large slope. Specifically, the VBM in the right side region (about 3 u.c.) of the ferroelectric barrier rises above the Fermi energy, which indicates the partial metallization in this area. However, in the right polarization state, the Fermi level is always located inside the band gap of the ferroelectric barrier. The above distributions of density of states lead to the great difference in the barrier width and the subsequent conductance between the left and right polarization states [Figs. 2(b) and 2(c)], which in turn gives rise to the giant TER effect. The electrostatic potential distribution as shown in Fig. 1(c) is consistent with the overall profile of the density of states in the two polarization states.

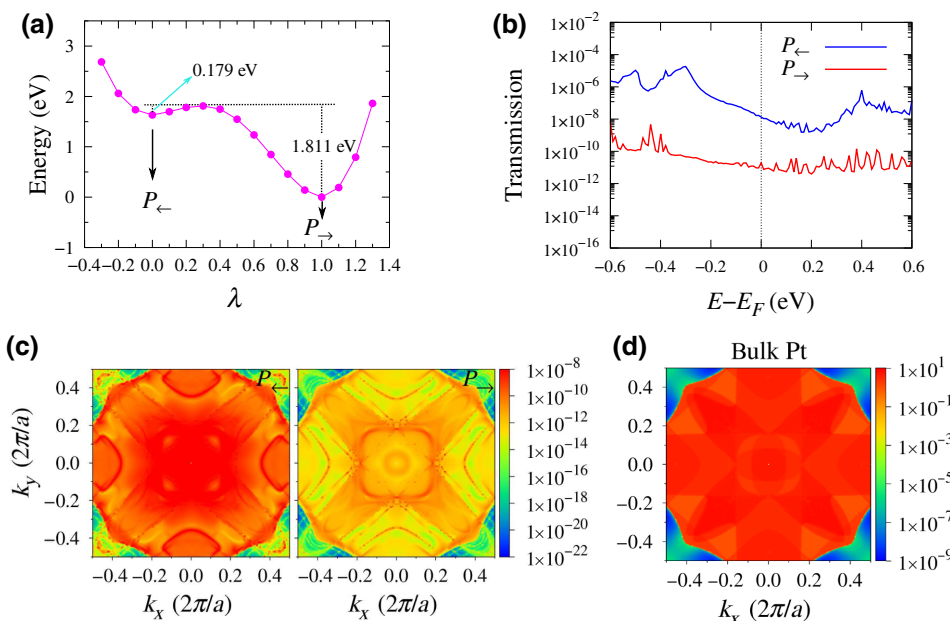


FIG. 2. Switching barriers and transmission functions for the  $\text{Na}_{\text{Ti}}\text{-FTJ}$  with 8.5 u.c.  $\text{BaTiO}_3$ . (a) The switching barriers between the two polarization states.  $\lambda = 0$  and  $\lambda = 1.0$  represent the left and right polarization state, respectively. (b) The  $k$ -averaged transmission of left ( $P_{\leftarrow}$ ) and right ( $P_{\rightarrow}$ ) polarization states as a function of energy  $E$ . (c) The  $k_{\parallel}$ -resolved transmission of left ( $P_{\leftarrow}$ ) and right ( $P_{\rightarrow}$ ) polarization states at the Fermi energy. (d) The  $k_{\parallel}$ -resolved transmission for bulk Pt electrode at the Fermi energy. For bulk Pt, the magnitude of transmission exactly reflects the density of Bloch states.

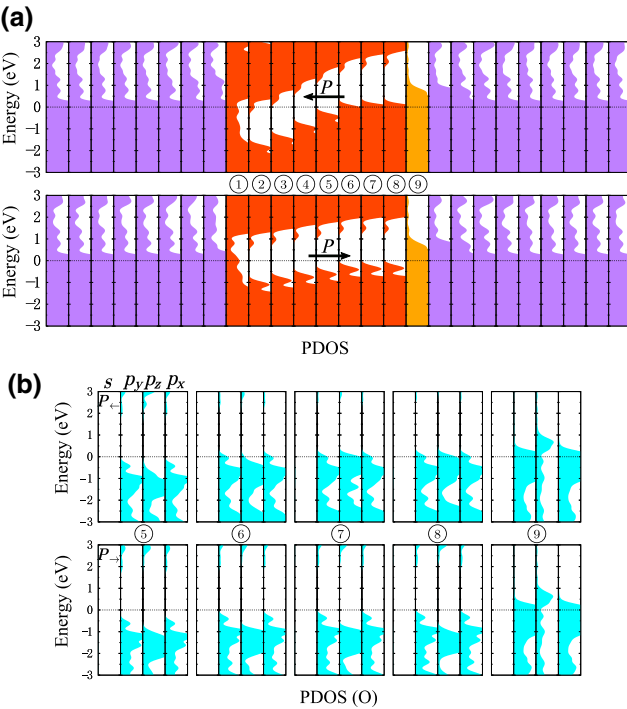


FIG. 3. Layer-resolved and orbital-resolved density of states for the  $\text{Na}_{\text{Ti}}$ -FTJ with 8.5 u.c.  $\text{BaTiO}_3$ . (a) The layer-resolved density of states of left polarization state ( $P_{\leftarrow}$ , top panel) and right polarization state ( $P_{\rightarrow}$ , bottom panel). Purple, orange, and yellow, respectively, represent the density of states of each atomic layer of Pt electrodes, the  $\text{TiO}_2$  atomic layers of  $\text{BaTiO}_3$ , and the  $\text{NaO}_2$  atomic layer at the right interface. The numbered circles in the middle identify the density of states in the  $\text{TiO}_2$  and  $\text{NaO}_2$  atomic layers. (b) The orbital-resolved density of states of O atoms of the numbered layers for the two polarization states.

To understand the mechanism of the partial metallization in the  $P_{\leftarrow}$  state, a schematic diagram is drawn in Fig. 4. If the negatively charged  $\text{NaO}_2$  layer is absent, the left polarization will induce a potential energy increase from left to right, followed by a small segment of drop induced by the one unit cell of right polarization close to the right interface [see the dashed line in Fig. 4(a)]. When the negatively charged  $\text{NaO}_2$  layer is taken into account, the electrical field induced by it will push the electron in the whole  $\text{BaTiO}_3$  barrier to higher energy. Particularly, the closer to the  $\text{NaO}_2$  layer, the larger increase in the potential energy the electrons will get (with an increase of  $\Delta V$  at the right interface), resulting in greatly increased slope of the potential energy profile. Near the right interface, the electron energy gets higher than the Fermi level [see the solid line in Fig. 4(a)], which leads to partial metallization of the right  $\text{BaTiO}_3$  unit cells (the right relatively flat segment indicates the partial metallization region). In the right polarization state, the potential energy profile induced by the ferroelectric polarization of  $\text{BaTiO}_3$  alone will decrease from left to right [see the dashed line in

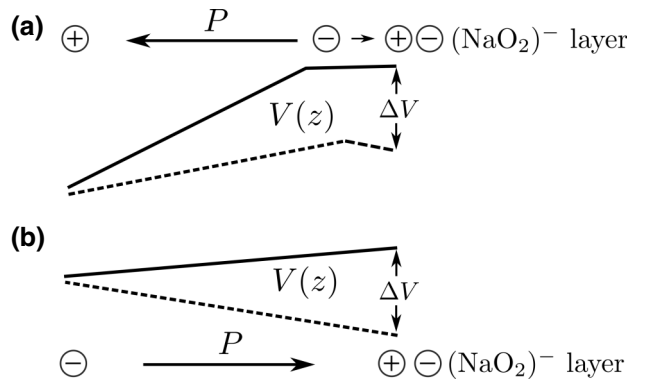


FIG. 4. Schematic diagram of potential energy increase induced by the negatively charged  $(\text{NaO}_2)^-$  layer for states: (a)  $P_{\leftarrow}$ ; (b)  $P_{\rightarrow}$ . The dashed lines indicate the potential energy induced by the ferroelectric polarization  $P_{\leftarrow/\rightarrow}$ , while the solid lines indicate the final potential energy after taking the potential energy increase  $\Delta V$  induced by the  $(\text{NaO}_2)^-$  layer into account. Here the superscript “-” of  $(\text{NaO}_2)^-$  only means it is negatively charged and does not mean the exact valence.

Fig. 4(b)]. However, due to the negatively charged  $\text{NaO}_2$  layer, it will also push the electron at the right interface to higher energy by  $\Delta V$  [see the solid line in Fig. 4(b)], changing the slope from negative to positive. This is why we see the large and small increases in Fig. 3(a) in the two polarization states. The small positive slope in Fig. 4(b) is not enough to raise the electron energy to be above the Fermi level, thus the whole  $\text{BaTiO}_3$  is still insulating.

Note that although the Na-doping scheme at the right interface is similar to the CoO layer insertion of Jiang *et al.*'s scheme [67] in achieving asymmetry in the  $\text{BaTiO}_3$  barrier, the effects of Na doping and CoO layer are greatly different. First, the role of the CoO layer at the right interface is to generate a very strong local polarization and a strong local field to push the conduction-band minimum (CBM) of the  $\text{BaTiO}_3$  barrier all below the Fermi level so as to achieve entire metallization, while the role of Na doping is to generate a negatively charged  $\text{NaO}_2$  surface, which induces a Coulomb potential and raises the VBM of the right region of the  $\text{BaTiO}_3$  barrier above the Fermi level and thus leads to partial metallization. Second, the Na doping avoids the necessity of a two-step process as required in the CoO layer scheme in which a first mechanical manipulation is used to turn the metallic state into an insulating state, followed by an electrical manipulation to revert the polarization.

By further analysis of the orbital-resolved density of states of the right half of the ferroelectric barrier [Fig. 3(b)], we find that the  $p_z$  orbital of O atoms dominates the high tunneling conductance in the left polarization state. This is because the  $p_z$  orbital of the O atom is along the transport direction, and there are orbitals, namely,  $d_{z^2}$ , along the same direction and not orthogonalized with the

$p_z$  orbital of O in the bulk Pt electrode [see Fig. S1 within the Supplemental Material [56]]. However, both  $p_x$  and  $p_y$  of the O atoms are localized in the  $x$ - $y$  plane and thus have no contribution to the conductance. After analyzing the calculation results, we also draw the following conclusions. For the two polarization states, since the orbitals of Ti atoms in the  $\text{TiO}_2$  atomic layers are basically located above the Fermi energy, there is almost no contribution to the conductance of the tunnel junction (Fig. S2 within the Supplemental Material [56]). Even if the density of states of Ti atoms in the second layer of the left polarization state drops below the Fermi energy, it does not contribute to the conductance because it has the symmetry of  $d_{xy}$  and is localized in the  $x$ - $y$  plane [Fig. S2(a) within the Supplemental Material [56]]. In addition, the Ba atoms and Na atoms do not contribute to conductance because they have only one  $s$  valence electron and its density of states around the Fermi energy is extremely small. The  $p_z$  orbitals of the O atoms in the BaO atomic layers that contribute to the conductance of the tunnel junction are all below the Fermi energy in both polarization states, so these O atoms almost do not participate in the transport of the tunnel junction (Fig. S3 within the Supplemental Material [56]).

We draw the charge-density distribution of two polarization states in real space by integrating LDOS between  $E_F - 0.1$  eV and  $E_F$  to obtain a more intuitive difference between them. It can be seen from Fig. 5(a) that the accumulation of charge density appears in the right interface region of the left polarization state, which is consistent with the PDOS distribution of the left polarization state in Fig. 3(a). Therefore, the thickness of the barrier in the left polarization state is correspondingly thinner, which enhances the conductance, and the charge density at this right interface region is mainly composed of O- $p$  orbitals [Fig. 3(b)]. However, for the right polarization state, very little charge density is shown in the entire barrier, which is consistent with the PDOS distribution for the right polarization state in Fig. 3(a). Thus, the right polarization state has a low conductance. Figure 5(b) shows the scattering states of  $\bar{\Gamma}$  point ( $k_{\parallel} = 0$ ) at the Fermi level of the FTJ. It is seen that the scattering state of the right polarization state decays more rapidly than that of the left polarization state, which is consistent with the partial charge density and proves again that the left polarization state has a higher conductance than the right polarization state.

Moreover, in order to explore the effect of increasing the thickness of the ferroelectric barrier on the stability of the bistable state, we calculate the substitution of Ti atom by Na atom at the  $\text{BaTiO}_3/\text{Pt}$  interface for the  $\text{Pt}(4.0 \text{ u.c.})/\text{BaTiO}_3(9.5 \text{ u.c.})/\text{Pt}(4.5 \text{ u.c.})$  FTJ. Figures 6(a)–6(c) show the optimized atomic structure, the relative Ti-O displacement of each atomic layer and the averaged electrostatic potential profiles, respectively. These figures of  $\text{Na}_{\text{Ti}}\text{-FTJ}$  with 9.5 u.c.  $\text{BaTiO}_3$  all exhibit similar

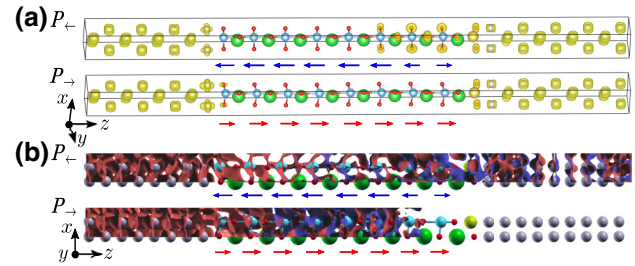


FIG. 5. Partial charge densities and real-space scattering states for the  $\text{Na}_{\text{Ti}}\text{-FTJ}$  with 8.5 u.c.  $\text{BaTiO}_3$  (primitive cell). (a) Partial charge densities in the left ( $P_{\leftarrow}$ ) and right ( $P_{\rightarrow}$ ) polarization states of the  $\text{Na}_{\text{Ti}}\text{-FTJ}$  with 8.5 u.c.  $\text{BaTiO}_3$ . The VESTA code [65] is used to visualize the isosurfaces with isovalues equal to 0.006. (b) The scattering states of left ( $P_{\leftarrow}$ ) and right ( $P_{\rightarrow}$ ) polarization states at the Fermi energy of this FTJ calculated by the Nanodal package [66]. The blue and red arrows correspond to the local polarization of  $\text{BaTiO}_3$  in the two polarization states.

characteristics to  $\text{Na}_{\text{Ti}}\text{-FTJ}$  with 8.5 u.c.  $\text{BaTiO}_3$ . As shown in Fig. 7(a), by using the same linear interpolation method of atomic coordinates as for the  $\text{Na}_{\text{Ti}}\text{-FTJ}$  with 8.5 u.c.  $\text{BaTiO}_3$ , we plot the energy barrier for the switching between the two polarization states of the  $\text{Na}_{\text{Ti}}\text{-FTJ}$  with 9.5 u.c.  $\text{BaTiO}_3$ . According to Fig. 7(a), the depth of the potential well for left polarization state increases to 0.242 eV (between  $\lambda = 0.0$  and 0.3) from 0.179 eV in the 8.5 u.c.  $\text{BaTiO}_3$  case, indicating the enhanced stability of the  $\text{Na}_{\text{Ti}}\text{-FTJ}$  with 9.5 u.c.  $\text{BaTiO}_3$  in the left polarization state. For the right polarization state of  $\text{Na}_{\text{Ti}}\text{-FTJ}$  with 9.5 u.c.  $\text{BaTiO}_3$ , the depth of the potential well is also slightly increased to 1.974 eV, as compared with the 1.811 eV in the 8.5 u.c.  $\text{BaTiO}_3$  case. It indicates that the increase of the thickness of the ferroelectric barrier helps to increase the stability of the two polarization states. This conclusion is consistent with the previous literature [64]. For this more stable bistable structure, we obtain a TER ratio of the same order of magnitude as the tunnel junction for  $\text{Na}_{\text{Ti}}\text{-FTJ}$  with 8.5 u.c.  $\text{BaTiO}_3$ , with a value of approximately  $2.755 \times 10^5\%$  [Fig. 7(b)]. This shows that we can increase the stability of the tunnel junction by increasing the thickness of the ferroelectric barrier while maintaining the TER ratio of the same order of magnitude. We also calculate the  $k_{\parallel}$ -resolved transmission (Fig. S4 within the Supplemental Material), layer-resolved density of states [Fig. S5(a) within the Supplemental Material] and orbital-resolved density of states [Fig. S5(b) within the Supplemental Material] of O atoms for the two polarization states of the  $\text{Na}_{\text{Ti}}\text{-FTJ}$  with 9.5 u.c.  $\text{BaTiO}_3$  [56], which all show similar characteristics to those of the  $\text{Na}_{\text{Ti}}\text{-FTJ}$  with 8.5 u.c.  $\text{BaTiO}_3$ .

Under the same calculation conditions, we study the effect of Ti substitution at the right interface by Li atom of the same main group as Na atom. For the  $\text{Li}_{\text{Ti}}\text{-FTJ}$  with 8.5 u.c.  $\text{BaTiO}_3$ , Fig. S6 within the Supplemental Material

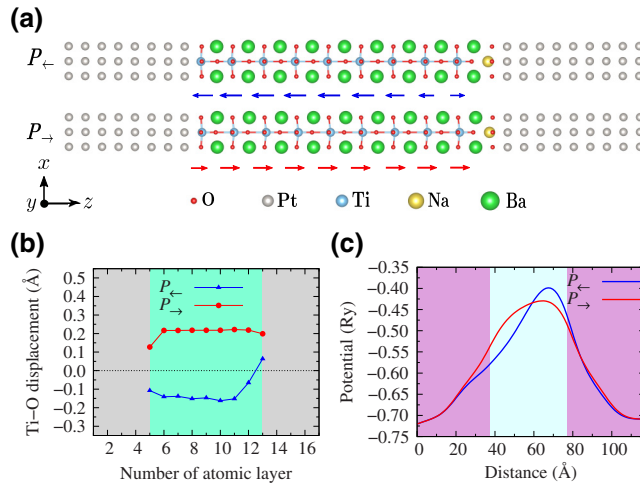


FIG. 6. Structural and polarization properties for the  $\text{Na}_{\text{Ti}}\text{-FTJ}$  with 9.5 u.c.  $\text{BaTiO}_3$ . (a) Schematic diagram of the optimized atomic structure of left polarization state ( $P_{\leftarrow}$ , top panel) and right polarization state ( $P_{\rightarrow}$ , bottom panel). The blue and red arrows correspond to the local polarization of  $\text{BaTiO}_3$  in the two polarization states. (b) The relative polar displacement between cation Ti and anion O in each atomic layer. (c) The averaged electrostatic potential distribution of the whole tunnel junction along the  $z$  direction.

shows its structure and polarization properties [56]. It is seen from Figs. S6(a, b) within the Supplemental Material that, compared with  $\text{Na}_{\text{Ti}}\text{-FTJ}$  with 8.5 u.c.  $\text{BaTiO}_3$ ,  $\text{Li}_{\text{Ti}}\text{-FTJ}$  with 8.5 u.c.  $\text{BaTiO}_3$  has two layers of polarization anomalies at the right interface under the left polarization state [56]. This is not conducive to the stability of the left polarization state. As shown in Fig. S7(a) within the Supplemental Material, the potential well in the left polarization state is only 0.078 eV [56]. However, as mentioned earlier, enhanced stability can be achieved by increasing the thickness of the ferroelectric layer. As shown in Fig. S7(b) within the Supplemental Material [56], we calculate the transport properties of  $\text{Li}_{\text{Ti}}\text{-FTJ}$  with 8.5 u.c.  $\text{BaTiO}_3$ ,

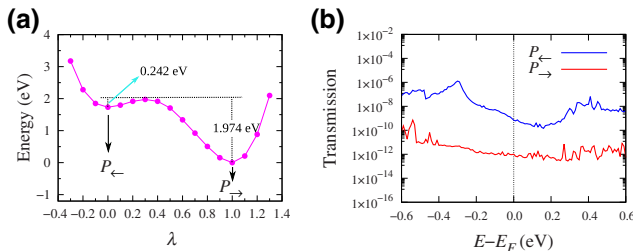


FIG. 7. The switching barriers and transmission functions for the  $\text{Na}_{\text{Ti}}\text{-FTJ}$  with 9.5 u.c.  $\text{BaTiO}_3$ . (a) The switching barriers between the two polarization states.  $\lambda = 0$  and  $\lambda = 1.0$  represent the left and right polarization state, respectively. (b) The  $k$ -averaged transmission of left ( $P_{\leftarrow}$ ) and right ( $P_{\rightarrow}$ ) polarization states as a function of energy  $E$ .

and the TER ratio reached approximately  $1.024 \times 10^5\%$ , which has the same order of magnitude as that of  $\text{Na}_{\text{Ti}}\text{-FTJ}$ . The layer and orbital resolved density of states of  $\text{Li}_{\text{Ti}}\text{-FTJ}$  with 8.5 u.c.  $\text{BaTiO}_3$  are shown in Fig. S8 within the Supplemental Material [56]. It is noted that, unlike the  $\text{Na}_{\text{Ti}}\text{-FTJ}$ , the layer-resolved density of states of three layers at the right interface of the right polarization state of the  $\text{Li}_{\text{Ti}}\text{-FTJ}$  rises above the Fermi level. However, by the analysis of the orbital-resolved density of states, these states are mainly contributed by the  $p_y$  and  $p_x$  orbitals of O atom, which do not contribute to the conductance because they are confined to the  $x$ - $y$  plane.

#### IV. CONCLUSION

In conclusion, we propose to break the symmetrical electrostatic potential distribution of the tunnel junction by replacing Ti atoms with Na (or Li) atoms at one of the interfaces of  $\text{Pt}/\text{BaTiO}_3/\text{Pt}$  FTJ. The asymmetrical electrostatic potential profiles combined with the ferroelectric polarization reversal cause great variation to the density of states of the ferroelectric barrier in the two polarization states. For the left polarization state, the density of states in the right region of the ferroelectric barrier (about 3 u.c.) rises above the Fermi energy, leading to partial metallization in this region. However, in the right polarization state, the positive ferroelectric bound charges and the negatively charged  $\text{NaO}_2$  interface cancel each other on the right side of the ferroelectric barrier, thus the distribution of the density of states is much smoother. The difference of distribution of density of states in the two polarization states leads to the huge difference of conductance, and the TER ratio of approximately  $10^5\%$  is obtained. In addition, we also show that the stability of the two polarization states can be enhanced by increasing the thickness of the ferroelectric barrier, and the magnitude of the TER ratio is maintained. We note that the  $\text{Pt}/\text{BaTiO}_3/\text{Pt}$  junction has been flagged as a pathological case within DFT due to the spurious band alignment between the materials [68], which may partly quantitatively affect the numerical accuracy of the results in this work. However, the interfacial doping proposed in this work can be extended to other systems and provides a feasible way for achieving large TER ratio, which will be helpful in the design of FTJs with good performance.

#### ACKNOWLEDGMENTS

We gratefully acknowledge the financial support by the National Natural Science Foundation of China (Grants No. 11974355 and No. 12074230), the National Key R&D Program of China (Grant No. 2017YFA0304203), Shanxi Province 100-Plan Talent Program and Fund for Shanxi “1331 Project,” and the Natural Science Foundation of

Jiangxi Province (Grant No. 20202ACBL212005). Calculations are performed at the Center for Computational Science of CASHIPS, the ScGrid of Supercomputing Center and the Computer Network Information Center of Chinese Academy of Sciences.

- 
- [1] E. Y. Tsymbal and H. Kohlstedt, Tunneling across a ferroelectric, *Science* **313**, 181 (2006).
- [2] M. Y. Zhuravlev, R. F. Sabirianov, S. S. Jaswal, and E. Y. Tsymbal, Giant Electroresistance in Ferroelectric Tunnel Junctions, *Phys. Rev. Lett.* **94**, 246802 (2005).
- [3] H. Kohlstedt, N. A. Pertsev, J. Rodríguez Contreras, and R. Waser, Theoretical current-voltage characteristics of ferroelectric tunnel junctions, *Phys. Rev. B* **72**, 125341 (2005).
- [4] A. Chanthbouala, A. Crassous, V. Garcia, K. Bouzehouane, S. Fusil, X. Moya, J. Allibe, B. Dlubak, J. Grollier, S. Xavier, C. Deranlot, A. Moshar, R. Proksch, N. D. Mathur, M. Bibes, and A. Barthélémy, Solid-state memories based on ferroelectric tunnel junctions, *Nat. Nanotechnol.* **7**, 101 (2012).
- [5] D. J. Kim, H. Lu, S. Ryu, C.-W. Bark, C.-B. Eom, E. Y. Tsymbal, and A. Gruverman, Ferroelectric tunnel memristor, *Nano Lett.* **12**, 5697 (2012).
- [6] V. Garcia and M. Bibes, Ferroelectric tunnel junctions for information storage and processing, *Nat. Commun.* **5**, 4289 (2014).
- [7] J. P. Velev, J. D. Burton, M. Y. Zhuravlev, and E. Y. Tsymbal, Predictive modelling of ferroelectric tunnel junctions, *Npj Comput. Mater.* **2**, 16009 (2016).
- [8] S. Boyn, S. Girod, V. Garcia, S. Fusil, S. Xavier, C. Deranlot, H. Yamada, C. Carrétéró, E. Jacquet, M. Bibes, A. Barthélémy, and J. Grollier, High-performance ferroelectric memory based on fully patterned tunnel junctions, *Appl. Phys. Lett.* **104**, 052909 (2014).
- [9] M. Abuwasib, H. Lu, T. Li, P. Buragohain, H. Lee, C.-B. Eom, A. Gruverman, and U. Singisetti, Scaling of electroresistance effect in fully integrated ferroelectric tunnel junctions, *Appl. Phys. Lett.* **108**, 152904 (2016).
- [10] L. Esaki, R. B. Laibowitz, and P. J. Stiles, Polar switch, *IBM Tech. Disc. Bull.* **13**, 2161 (1971).
- [11] J. Junquera and P. Ghosez, Critical thickness for ferroelectricity in perovskite ultrathin films, *Nature* **422**, 506 (2003).
- [12] D. D. Fong, G. B. Stephenson, S. K. Streiffer, J. A. Eastman, O. Auciello, P. H. Fuoss, and C. Thompson, Ferroelectricity in ultrathin perovskite films, *Science* **304**, 1650 (2004).
- [13] N. Sai, A. M. Kolpak, and A. M. Rappe, Ferroelectricity in ultrathin perovskite films, *Phys. Rev. B* **72**, 020101(R) (2005).
- [14] M. Dawber, K. M. Rabe, and J. F. Scott, Physics of thin-film ferroelectric oxides, *Rev. Mod. Phys.* **77**, 1083 (2005).
- [15] P. W. M. Blom, R. M. Wolf, J. F. M. Cillessen, and M. P. C. M. Krijn, Ferroelectric Schottky Diode, *Phys. Rev. Lett.* **73**, 2107 (1994).
- [16] A. Q. Jiang, C. Wang, K. J. Jin, X. B. Liu, J. F. Scott, C. S. Hwang, T. A. Tang, H. B. Lu, and G. Z. Yang, A resistive memory in semiconducting BiFeO<sub>3</sub> thin-film capacitors, *Adv. Mater.* **23**, 1277 (2011).
- [17] L. Kang, P. Jiang, H. Hao, Y. Zhou, X. Zheng, L. Zhang, and Z. Zeng, Giant tunneling electroresistance in two-dimensional ferroelectric tunnel junctions with out-of-plane ferroelectric polarization, *Phys. Rev. B* **101**, 014105 (2020).
- [18] L. Kang, P. Jiang, H. Hao, Y. Zhou, X. Zheng, L. Zhang, and Z. Zeng, Giant tunnel electroresistance in ferroelectric tunnel junctions with metal contacts to two-dimensional ferroelectric materials, *Phys. Rev. B* **103**, 125414 (2021).
- [19] W. Xiao, L. Kang, H. Hao, Y. Zhou, L. Zhang, X. Zheng, and Z. Zeng, Giant tunneling electroresistance arising from reversible partial barrier metallization in the NaTiO<sub>3</sub>/BaTiO<sub>3</sub>/LaTiO<sub>3</sub> ferroelectric tunnel junction, *Phys. Chem. Chem. Phys.* **23**, 16349 (2021).
- [20] V. Garcia, S. Fusil, K. Bouzehouane, S. Enouz-Vedrenne, N. D. Mathur, A. Barthélémy, and M. Bibes, Giant tunnel electroresistance for non-destructive readout of ferroelectric states, *Nature* **460**, 81 (2009).
- [21] A. Gruverman, D. Wu, H. Lu, Y. Wang, H. W. Jang, C. M. Folkman, M. Y. Zhuravlev, D. Felker, M. Rzchowski, C.-B. Eom, and E. Y. Tsymbal, Tunneling electroresistance effect in ferroelectric tunnel junctions at the nanoscale, *Nano Lett.* **9**, 3539 (2009).
- [22] P. Maksymovych, S. Jesse, P. Yu, R. Ramesh, A. P. Badorf, and S. V. Kalinin, Polarization control of electron tunneling into ferroelectric surfaces, *Science* **324**, 1421 (2009).
- [23] Z. Wen, C. Li, D. Wu, A. Li, and N. Ming, Ferroelectric-field-effect-enhanced electroresistance in metal/ferroelectric/semiconductor tunnel junctions, *Nat. Mater.* **12**, 617 (2013).
- [24] H. Lu, A. Lipatov, S. Ryu, D. J. Kim, H. Lee, M. Y. Zhuravlev, C. B. Eom, E. Y. Tsymbal, A. Sinitskii, and A. Gruverman, Ferroelectric tunnel junctions with graphene electrodes, *Nat. Commun.* **5**, 5518 (2014).
- [25] S. Boyn, A. M. Douglas, C. Blouzon, P. Turner, A. Barthélémy, M. Bibes, S. Fusil, J. M. Gregg, and V. Garcia, Tunnel electroresistance in BiFeO<sub>3</sub> junctions: Size does matter, *Appl. Phys. Lett.* **109**, 232902 (2016).
- [26] Z. Xi, J. Ruan, C. Li, C. Zheng, Z. Wen, J. Dai, A. Li, and D. Wu, Giant tunnelling electroresistance in metal/ferroelectric/semiconductor tunnel junctions by engineering the Schottky barrier, *Nat. Commun.* **8**, 15217 (2017).
- [27] N. W. Ashcroft and N. D. Mermin, *Solid State Physics* (Saunders College Publishing, New York, 1976).
- [28] F. Y. Bruno, S. Boyn, S. Fusil, S. Girod, C. Carrétéró, M. Marinova, A. Gloter, S. Xavier, C. Deranlot, M. Bibes, A. Barthélémy, and V. Garcia, Millionfold resistance change in ferroelectric tunnel junctions based on nickelate electrodes, *Adv. Electron. Mater.* **2**, 1500245 (2016).
- [29] H. Yamada, V. Garcia, S. Fusil, S. Boyn, M. Marinova, A. Gloter, S. Xavier, J. Grollier, E. Jacquet, C. Carrétéró, C. Deranlot, M. Bibes, and A. Barthélémy, Giant electroresistance of super-tetragonal BiFeO<sub>3</sub>-based ferroelectric tunnel junctions, *ACS Nano* **7**, 5385 (2013).
- [30] S. Boyn, V. Garcia, S. Fusil, C. Carrétéró, K. Garcia, S. Xavier, S. Collin, C. Deranlot, M. Bibes, and A. Barthélémy, Engineering ferroelectric tunnel junctions

- through potential profile shaping, *APL Mater.* **3**, 061101 (2015).
- [31] D. Griffiths, *Introduction to Quantum Mechanics* (Pearson Prentice Hall, Upper Saddle River, NJ, USA, 2005).
- [32] X. Liu, J. D. Burton, and E. Y. Tsymbal, Enhanced Tunneling Electroresistance in Ferroelectric Tunnel Junctions due to the Reversible Metallization of the Barrier, *Phys. Rev. Lett.* **116**, 197602 (2016).
- [33] D. I. Bilec, F. D. Novaes, J. Íñiguez, P. Ordejón, and P. Ghosez, Electroresistance effect in ferroelectric tunnel junctions with symmetric electrodes, *ACS Nano* **6**, 1473 (2012).
- [34] A. Quindeau, V. Borisov, I. Fina, S. Ostanin, E. Pippel, I. Mertig, D. Hesse, and M. Alexe, Origin of tunnel electroresistance effect in  $\text{PbTiO}_3$ -based multiferroic tunnel junctions, *Phys. Rev. B* **92**, 035130 (2015).
- [35] E. Dagotto, T. Hotta, and A. Moreo, Colossal magnetoresistant materials: The key role of phase separation, *Phys. Rep.* **344**, 1 (2001).
- [36] P. Schiffer, A. P. Ramirez, W. Bao, and S.-W. Cheong, Low Temperature Magnetoresistance and the Magnetic Phase Diagram of  $\text{La}_{1-x}\text{Ca}_x\text{MnO}_3$ , *Phys. Rev. Lett.* **75**, 3336 (1995).
- [37] J. D. Burton and E. Y. Tsymbal, Prediction of electrically induced magnetic reconstruction at the manganite/ferroelectric interface, *Phys. Rev. B* **80**, 174406 (2009).
- [38] Y. W. Yin, J. D. Burton, Y.-M. Kim, A. Y. Borisevich, S. J. Pennycook, S. M. Yang, T. W. Noh, A. Gruverman, X. G. Li, E. Y. Tsymbal, and Q. Li, Enhanced tunnelling electroresistance effect due to a ferroelectrically induced phase transition at a magnetic complex oxide interface, *Nat. Mater.* **12**, 397 (2013).
- [39] L. Jiang, W. S. Choi, H. Jeen, S. Dong, Y. Kim, M.-G. Han, Y. Zhu, S. V. Kalinin, E. Dagotto, T. Egami, and H. N. Lee, Tunneling electroresistance induced by interfacial phase transitions in ultrathin oxide heterostructures, *Nano Lett.* **13**, 5837 (2013).
- [40] G. Radaelli, D. Gutiérrez, M. Qian, I. Fina, F. Sánchez, L. Baldrati, J. Heidler, C. Piamonteze, R. Bertacco, and J. Fontcuberta, Strain-controlled responsiveness of slave half-doped manganite  $\text{La}_{0.5}\text{Sr}_{0.5}\text{MnO}_3$  layers inserted in  $\text{BaTiO}_3$  ferroelectric tunnel junctions, *Adv. Electron. Mater.* **2**, 1600368 (2016).
- [41] W. J. Hu, Z. Wang, W. Yu, and T. Wu, Optically controlled electroresistance and electrically controlled photovoltage in ferroelectric tunnel junctions, *Nat. Commun.* **7**, 10808 (2016).
- [42] J. Li, N. Li, C. Ge, H. Huang, Y. Sun, P. Gao, M. He, C. Wang, G. Yang, and K. Jin, Giant electroresistance in ferroionic tunnel junctions, *iScience* **16**, 368 (2019).
- [43] R. Soni, A. Petraru, P. Meuffels, O. Vavra, M. Ziegler, S. K. Kim, D. S. Jeong, N. A. Pertsev, and H. Kohlstedt, Giant electrode effect on tunnelling electroresistance in ferroelectric tunnel junctions, *Nat. Commun.* **5**, 5414 (2014).
- [44] C. Yoon, J. H. Lee, S. Lee, J. H. Jeon, J. T. Jang, D. H. Kim, Y. H. Kim, and B. H. Park, Synaptic plasticity selectively activated by polarization-dependent energy-efficient ion migration in an ultrathin ferroelectric tunnel junction, *Nano Lett.* **17**, 1949 (2017).
- [45] M. Y. Zhuravlev, Y. Wang, S. Maekawa, and E. Y. Tsymbal, Tunneling electroresistance in ferroelectric tunnel junctions with a composite barrier, *Appl. Phys. Lett.* **95**, 052902 (2009).
- [46] Y.-Z. Wu, S. Ju, and Z.-Y. Li, Effects of electrodes and space charges on the tunneling electroresistance in the ferroelectric tunnel junction with a  $\text{SrTiO}_3/\text{BaTiO}_3$  composite barrier, *Appl. Phys. Lett.* **96**, 252905 (2010).
- [47] L. Wang, M. R. Cho, Y. J. Shin, J. R. Kim, S. Das, J.-G. Yoon, J.-S. Chung, and T. W. Noh, Overcoming the fundamental barrier thickness limits of ferroelectric tunnel junctions through  $\text{BaTiO}_3/\text{SrTiO}_3$  composite barriers, *Nano Lett.* **16**, 3911 (2016).
- [48] T. Li, P. Sharma, A. Lipatov, H. Lee, J.-W. Lee, M. Y. Zhuravlev, T. R. Paudel, Y. A. Genenko, C.-B. Eom, E. Y. Tsymbal, A. Sinitskii, and A. Gruverman, Polarization-mediated modulation of electronic and transport properties of hybrid  $\text{MoS}_2\text{-BaTiO}_3\text{-SrRuO}_3$  tunnel junctions, *Nano Lett.* **17**, 922 (2017).
- [49] A. Leitner, C. T. Rogers, J. C. Price, D. A. Rudman, and D. R. Herman, Pulsed laser deposition of superconducting Nb-doped strontium titanate thin films, *Appl. Phys. Lett.* **72**, 3065 (1998).
- [50] R. Moos, S. Schöllhammer, and K. H. Härdtl, Electron mobility of  $\text{Sr}_{1-x}\text{La}_x\text{TiO}_3$  ceramics between 600°C and 1300°C, *Appl. Phys. A: Mater. Sci. Process.* **65**, 291 (1997).
- [51] S. Ohta, T. Nomura, H. Ohta, M. Hirano, H. Hosono, and K. Koumoto, Large thermoelectric performance of heavily Nb-doped  $\text{SrTiO}_3$  epitaxial film at high temperature, *Appl. Phys. Lett.* **87**, 092108 (2005).
- [52] N. Shanthi and D. D. Sarma, Electronic structure of electron doped  $\text{SrTiO}_3$ :  $\text{SrTiO}_{3-\delta}$  and  $\text{Sr}_{1-x}\text{La}_x\text{TiO}_3$ , *Phys. Rev. B* **57**, 2153 (1998).
- [53] C. Zhang, C. L. Wang, J. C. Li, K. Yang, Y. F. Zhang, and Q. Z. Wu, Substitutional position and insulator-to-metal transition in Nb-doped  $\text{SrTiO}_3$ , *Mater. Chem. Phys.* **107**, 215 (2008).
- [54] Z. Wang, S. Tsukimoto, M. Saito, and Y. Ikuhara, Quantum electron transport through  $\text{SrTiO}_3$ : Effects of dopants on conductance channel, *Appl. Phys. Lett.* **94**, 252103 (2009).
- [55] K. Klyukin, L. L. Tao, E. Y. Tsymbal, and V. Alexandrov, Defect-Assisted Tunneling Electroresistance in Ferroelectric Tunnel Junctions, *Phys. Rev. Lett.* **121**, 056601 (2018).
- [56] See Supplemental Material at <http://link.aps.org/supplemental/10.1103/PhysRevApplied.17.044001> for other detailed information.
- [57] L. Shen, T. Zhou, Z. Bai, M. Zeng, J. Q. Goh, Z.-m. Yuan, G. Han, B. Liu, and Y. P. Feng, Systematic study of ferroelectric, interfacial, oxidative, and doping effects on conductance of  $\text{Pt}/\text{BaTiO}_3/\text{Pt}$  ferroelectric tunnel junctions, *Phys. Rev. B* **85**, 064105 (2012).
- [58] J. P. Velev, C.-G. Duan, K. D. Belashchenko, S. S. Jaswal, and E. Y. Tsymbal, Effect of Ferroelectricity on Electron Transport in  $\text{Pt}/\text{BaTiO}_3/\text{Pt}$  Tunnel Junctions, *Phys. Rev. Lett.* **98**, 137201 (2007).
- [59] D. Sánchez-Portal, P. Ordejón, E. Artacho, and J. M. Soler, Density-functional method for very large systems with LCAO basis sets, *Int. J. Quantum Chem.* **65**, 453 (1997).
- [60] J. M. Soler, E. Artacho, J. D. Gale, A. García, J. Junquera, P. Ordejón, and D. Sánchez-Portal, The SIESTA method for

- ab initio order- $N$  materials simulation, *J. Phys.: Condens. Matter* **14**, 2745 (2002).
- [61] J. P. Perdew, K. Burke, and M. Ernzerhof, Generalized Gradient Approximation Made Simple, *Phys. Rev. Lett.* **77**, 3865 (1996).
- [62] M. Brandbyge, J.-L. Mozo, P. Ordejón, J. Taylor, and K. Stokbro, Density-functional method for nonequilibrium electron transport, *Phys. Rev. B* **65**, 165401 (2002).
- [63] N. Papior, N. Lorente, T. Frederiksen, A. García, and M. Brandbyge, Improvements on non-equilibrium and transport Green function techniques: The next-generation TRANSIESTA, *Comput. Phys. Commun.* **212**, 8 (2017).
- [64] Q. Yang, L. Tao, Y. Zhang, M. Li, Z. Jiang, E. Y. Tsymbal, and V. Alexandrov, Ferroelectric tunnel junctions enhanced by a polar oxide barrier layer, *Nano Lett.* **19**, 7385 (2019).
- [65] K. Momma and F. Izumi, VESTA: A three-dimensional visualization system for electronic and structural analysis, *J. Appl. Crystallogr.* **41**, 653 (2008).
- [66] J. Taylor, H. Guo, and J. Wang, Ab initio modeling of quantum transport properties of molecular electronic devices, *Phys. Rev. B* **63**, 245407 (2001).
- [67] L. N. Jiang, W. Z. Chen, B. S. Yang, X.-G. Zhang, Y.-P. Wang, and X. F. Han, First-principles prediction of switchable metallic ferroelectricity in multi-ferroic tunnel junctions, *Phys. Rev. B* **99**, 224103 (2019).
- [68] M. Stengel, P. Aguado-Puente, N. A. Spaldin, and J. Junquera, Band alignment at metal/ferroelectric interfaces: Insights and artifacts from first principles, *Phys. Rev. B* **83**, 235112 (2011).